

## Confirming Near- to Mid-IR Photometrically-Identified Obscured AGNs in the JWST era

GEORGE H. RIEKE,<sup>1</sup> YANG SUN,<sup>1</sup> JIANWEI LYU,<sup>1</sup> CHRISTOPHER N. A. WILLMER,<sup>1</sup> YONGDA ZHU,<sup>1</sup> PIERLUIGI RINALDI,<sup>1</sup>  
MEREDITH A. STONE,<sup>1</sup> KEVIN N. HAINLINE,<sup>1</sup> AND PABLO G. PÉREZ-GONZÁLEZ<sup>2</sup>

<sup>1</sup>*Steward Observatory, University of Arizona, 933 North Cherry Avenue, Tucson, AZ 85721, USA*

<sup>2</sup>*Centro de Astrobiología (CAB), CSIC-INTA, Ctra. de Ajalvir km 4, Torrejón de Ardoz, E-28850, Madrid, Spain*

### ABSTRACT

We evaluate the underlying assumptions for the identification of Active Galactic Nuclei (AGNs) through near- and mid-infrared photometry and spectral energy distribution (SED) fitting out to  $z \sim 3$ . For massive galaxies,  $\log(M) \geq 9.5$ , our high resolution spectra of the rest optical range generally confirm the results of SED fitting, which relies primarily on excesses above the stellar emission between 1 and 6  $\mu\text{m}$  to identify AGN. However, the method is undermined if the redshift used for the SED fitting is incorrect. Low mass galaxies,  $\log(M) < 9.5$ , can contain relatively warm dust that emits in the 4 - 6  $\mu\text{m}$  range. We show that the potential contamination of AGN samples by purely star forming low-mass galaxies can be avoided by the use of the infrared properties of Haro 11 as a limiting star-forming SED template. However, relatively few star forming galaxies emit as strongly in the 3–6  $\mu\text{m}$  range as this template, so this could result in missing some obscured AGNs to avoid a minor contamination. Including the behavior of the galaxies at rest  $\lambda \sim 13.5 \mu\text{m}$  can mitigate this problem and yield more complete samples of *bona fide* AGN. JWST/MIRI supports this approach out to  $z \lesssim 0.6$ .

### 1. INTRODUCTION

Two recent review articles, Hickox & Alexander (2018); Lyu & Rieke (2022), have emphasized that mid-infrared observations are critical to find complete samples of heavily dust-obscured AGNs. They describe large-scale searches using data from IRAS, ISO, Spitzer, and WISE. With the advent of JWST, such searches have been extended to higher redshifts, much lower luminosities, and more sophisticated analyses to take advantage of the sensitivity and many mid-infrared bands provided by the Mid-Infrared Instrument (MIRI) (Yang et al. 2023; Kirkpatrick et al. 2023; Lyu et al. 2024; Li et al. 2024; Chien et al. 2024).

These JWST surveys push the AGN mid-infrared selection into previously unexplored realms. The assumption behind the new surveys is that the infrared emission powered by star formation should exhibit strong mid-infrared Polycyclic Aromatic Hydrocarbon (PAH) features. PAH features do not emit strongly at wavelengths short of 6  $\mu\text{m}$  (excepting a moderately strong feature at 3.3  $\mu\text{m}$ ) and even obscured AGNs do emit in this range. This difference is the foundation of traditional obscured AGN identification via mid-infrared SED fitting using templates including the PAH bands. This approach should be robust so long as accurate redshifts are available and any infrared excess powered by young stars is PAH-dominated and not so strong that it overwhelms the AGN contribution.

As an example, Lyu et al. (2024) conducted a comprehensive search for AGN in SMILES. This is a MIRI survey of a central region in the GOODS-S field and coincides with the JADES/NIRCam survey from 0.9 to 5  $\mu\text{m}$  (plus deep Chandra, HST, ALMA, and JVLA data); see Rieke et al. (2024) for a description. For  $M_{\text{host}} > 5 \times 10^9 M_{\odot}$ , a PAH - based template is appropriate to fit stellar-powered infrared emission (Shivaei et al. 2024). Lyu et al. (2024) used such a template to characterize infrared emission from host galaxies with  $M_{\text{host}} > 5 \times 10^9 M_{\odot}$  and found 111 AGN candidates. This was facilitated because SMILES includes all the MIRI bands from 5.6 through 25.5  $\mu\text{m}$  with integration times selected to identify PAH features and support this type of study (Rieke et al. 2024).

SED fitting with MIRI photometry also reveals a large number of AGN candidates in lower-mass galaxies: Lyu et al. (2024) identified 86 candidates ( $\sim 2 \text{ arcmin}^{-2}$ ), whereas Yang et al. (2023) found even more. However, confirming their nature from photometry alone is challenging, since local low-mass, dwarf galaxies have weak PAH emission, due to destruction by the hard interstellar radiation fields (e.g., Hunt et al. 2010) and also can have a warm non-PAH infrared component (e.g., Wu et al. 2006; Rémy-Ruyer et al. 2015) whose emission extends short of 6  $\mu\text{m}$ . This warm emission arises because of their hard interstellar radiation fields, the porous structure of their ISMs (Madden et al. 2016) that

allows these fields to penetrate efficiently, and because their dust contains very small grains, for example from shattering by shocks (see discussion in the review by Hunter et al. (2024)). In a study of local star-forming galaxies with  $M_* < 3 \times 10^9 M_\odot$ , Hainline et al. (2016) found the extreme case is defined by a number of galaxies with significant excesses even in WISE  $W1 - W2$ , i.e., at  $4.6 \mu\text{m}$ . From these examples, they conclude that star formation can heat dust to temperatures where the emission can be confused with AGN heating.

Locally, the low-mass, hot-dust galaxies identified by Hainline et al. (2016) appear to be rare. Nonetheless, searches for obscured AGNs need to be aware of the possibility that a larger fraction of low-metallicity galaxies at the relevant redshifts may have sufficient hot dust to violate selection criteria based on PAH-inclusive star forming templates. At the same time, if hot dust examples are indeed rare even at these redshifts, selection methods need to be tuned so they do not reject a large number of true AGN to avoid a low level of contamination.

This paper examines the issues around AGN identification in both high-mass and low-mass galaxies. As part of the search for obscured AGN in the SMILES survey reported by Lyu et al. (2024), we obtained NIRSpec Micro Shutter Array (MSA) (Jakobsen et al. 2022) spectra of a small sample of objects. This sample was designed as a test of whether the source properties are as assumed in the photometric SED fitting. Specifically, we wanted to test whether (1) the star formation rates deduced from the spectra are consistent with those deduced from the SED fitting; and (2) the AGN emission lines are suppressed in the purported obscured sources, consistent with the level of obscuration. The spectra also give us an insight to the behavior of the SED fitting in identifying AGN at redshifts  $z > 2.5$ , where the aromatic features move out of the MIRI photometric bands. This paper will discuss these spectra in Section 3.

The second objective of the paper is an assessment of the risk that low metallicity galaxies can mimic AGNs in infrared photometry, leading to false identifications such as those discussed by Hainline et al. (2016). In Section 4, we will evaluate the behavior of local dwarf galaxies in AGN color selections and the prevalence of hot-dust SEDs that might be confused with AGNs. We suggest a suitable SED template where hot dust is suspected and then suggest a method to further refine mid-infrared photometric AGN searches to moderate redshift, using MIRI photometry. Finally, Section 5 discusses the issue of degeneracy in photometric AGN searches, followed by a concluding summary.

## 2. NIRSPEC OBSERVATIONS

As summarized in Zhu et al. (in prep), we have obtained JWST/NIRSpec MSA spectra of 166 galaxies as part of the SMILES survey (PID 1207, PI: Rieke; Alberts et al. 2024; Rieke et al. 2024) with the main goal to characterize the spectral properties of various MIRI sources. These galaxies were observed with the G140M/F100LP and G235M/F170LP gratings and blocking filters to cover  $0.97\text{-}3.07 \mu\text{m}$  in the observed frame ( $0.4\text{-}1.3 \mu\text{m}$  in the rest frame for a typical redshift in our sample) at a spectral resolution of  $R \sim 1000$ . The effective exposure time with each disperser/filter combination was 7,000 seconds ( $\sim 1.94$  hours). In this work, we focus on a subset of 17 MIRI-selected AGN candidates with  $z=1.24\text{-}3.33$  so that the [O III],  $H\beta$ , [N II] and  $H\alpha$  can be covered with the instrument setup.

We processed and calibrated the data using the JWST Calibration Pipeline (Bushouse et al. 2022), version 1.14.0, with the CRDS<sup>1</sup> context `jwst_1236.pmap`. In brief, the `calwebb_detector1` stage converted “uncal.fits” files into uncalibrated rate images. Next, the `calwebb_spec2` stage applied flat-field corrections, flux calibration, and local background subtraction, yielding resampled spectra for each nodding position. The final spectral combination and extraction were carried out using `calwebb_spec3`. Additionally, we applied custom scripts to further reject hot pixels and remove  $1/f$  noise. A detailed description of the reduction process, along with reduced spectra and the redshift catalog, will be provided in a forthcoming data release (Y. Zhu et al., in prep.; see also Zhu et al. 2025). The data can be accessed at doi=10.17909/et3f-zd57 and the spectra are displayed in the appendix.

The MSA shutters provide slitlets of size  $0.20 \times 0.46''$  in size. We did not apply a slit-loss correction for line ratio measurements in BPT diagrams to avoid any bias due emission lines having different morphologies in the galaxy images used for the correction. For  $H\alpha$  luminosity, however, we corrected for slit loss by comparing the flux within the MSA shutter to the total Kron-convolved photometry across multiple NIRCcam bands (F115W, F150W, and F210M), and we fit a second-order polynomial to model wavelength-dependent slit loss. Emission lines were measured using Gelato (Hviding 2022), from which line parameters (redshift, intensity, widths) were determined. The emission line template includes [OII]  $\lambda\lambda 3727\&3729$ , [OIII]  $\lambda\lambda 4959\&5007$ , [OI]  $\lambda\lambda 6302\&6365$ , [NII]  $\lambda\lambda 6549\&6585$ , [SII]  $\lambda\lambda 6718\&6732$ , and Balmer lines modeled by a single Gaussian component each. We

<sup>1</sup> Calibration Reference Data System: <https://jwst-crds.stsci.edu/>

used the spectroscopic redshift, based on all the lines well detected in the spectrum, as the input prior. A total of 17 galaxies that were identified as having obscured AGN from SED analysis (Lyu et al. 2024) were included in this analysis, selected to illustrate a range of behavior and redshift. Key emission lines and their ratios for these galaxies, along with the method of identifying AGNs and estimates of their metallicities, are summarized in Table 1.

### 3. ANALYSIS

#### 3.1. BPT Diagram

Figure 1 shows the galaxies with adequate signal to noise (SNR>3 for the BPT line ratios) placed on a BPT diagram. The blue points are for non-AGN galaxies with SMILES spectra at a similar redshift range, and they fall in the expected region. Only the 14 AGN galaxies with adequate signal to noise are plotted; 11/14 of these galaxies have line ratios consistent with star formation being the dominant excitation mechanism<sup>2</sup>. This is as expected for hosts of highly obscured AGN, where the UV radiation from the AGN is unable to escape an embedding dense cocoon and excite the interstellar gas outside.

The exceptions are IDs 196290 (B), possibly 87191 ([A]), and 209962 ([C]). The effect of lower metallicity at high redshift will shift the BPT demarcation line upward putting ID 87191 [A] on the line rather than above it. The classification of this galaxy as star-forming is consistent with its spectrum (Figure 1), which indicates an inflow or outflow that broadens the [OIII] lines. ID 196290 (B) shows a broad component in its H $\alpha$  line, although the SED implies that much of the output of its AGN is absorbed and re-emitted in the infrared. ID 209962 shows a lightly obscured Type 1 AGN continuum, but the presence of a high velocity [OIII] outflow and the weakness of its H $\beta$  line preclude a sensitive search for a broad line region. To quantify the broad components that we see in the spectra of ID 87191, 196290, and 209962, we re-fit their broad lines ([OIII] for ID 87191 and 209962, H $\alpha$  for ID 196290) using multiple Gaussian components. The narrow component is fixed at the systemic redshift and its width is only restricted within 500 km/s. The broad component is allowed to be blue/red-shifted and must have a width wider than the

narrow component. The best fits and the width of the broad component(s) of the three galaxies are shown in the right panel of Figure 1.

#### 3.2. Star Formation rate estimates

Our estimation of star formation rates from H $\alpha$  follows the procedure outlined in Kennicutt & Evans (2012), determining extinction to H $\alpha$  as in Koyama et al. (2015), Equation 3. This latter approach originated in Calzetti (2001); updating the extinction coefficients according to Momcheva et al. (2013) gives close agreement to the equation used in Koyama et al. (2015). Details are provided in the Appendix. In some cases, the spectra indicate large Balmer decrements; if these are interpreted in terms of extinction, the derived SFR substantially exceeds a plausible level relative to the galaxy main sequence. It may be, for example, that there is H $\beta$  absorption in the stellar continuum, reducing the apparent emission line strength. These cases are noted in the footnotes. The SFRs from H $\alpha$  are mildly dependent on metallicity/redshift (Backhaus et al. 2024) but not sufficiently to affect our analysis.

The SFRs from the spectra are reported in Table 2, which also lists the SFRs estimated from fitting the spectral energy distribution using *Prospector* (Johnson et al. 2021) as carried out by Lyu et al. (2024) to identify AGNs in these systems. The details of the customized *Prospector* fitting are described in Lyu et al. (2022), Sections 3.1.1 and 3.1.2. and Lyu et al. (2024), Sections 3.1 and 3.2. We have carried out new fits to take advantage of improved redshifts and reductions of the photometry.

For  $z \gtrsim 2.6$ , even the 6.2  $\mu\text{m}$  PAH band is at the long end (or beyond) the cutoff of the MIRI 21  $\mu\text{m}$  filter. Unless high signal to noise has been achieved at 25.5  $\mu\text{m}$ , the AGN identification can no longer be based on the absence of PAH emission. We have put the IDs of the seven galaxies with  $z \geq 2.6$  in italics in Table 2. For these cases, the identification of an AGN is based on the elevated SED at wavelengths  $< 6 \mu\text{m}$  above the expectations for stellar photospheric output and is independent of the SFR estimates.

#### 3.3. Individual galaxies

Here we discuss the galaxies in this study individually. Figure 2 shows the model fits for all 17 galaxies and is a useful reference for the discussion. Galaxy masses have been determined from the *Prospector* fits to the photometry. From Figure 2, in all but one case the short wavelengths are strongly dominated by the direct stellar emission, which is characterized by many photometric measurements allowing for accurate synthesis fits. For

<sup>2</sup> The diagram shifts modestly at the redshifts of these galaxies, but their values of  $z$  range by nearly a factor of three so this is difficult to show simply. However, all of them remain in the star forming zone since higher redshifts tend to move the lines of demarcation upward and to the right, i.e., away from the points and hence retains their classification as star-forming.

**Table 1.** Key lines and ratios

JADES	z	SMILES	AGN	H $\alpha$ <sup>c</sup>	err	H $\alpha$ /H $\beta$	err	[OIII] <sup>d</sup> /H $\beta$	err	[NII] <sup>e</sup> /H $\alpha$	err	Z $_{\odot}$ <sup>f</sup>
ID		ID <sup>a</sup>	Code <sup>b</sup>	10 <sup>-17</sup> W/m <sup>2</sup>								
87191 <sup>g</sup>	2.15	540	1	6.12	0.011	7.09	0.45	14.14	0.29	0.01	0.001	7.9
113325 <sup>g</sup>	2.49	2573	1	1.042	0.013	3.02	0.15	5.19	0.25	-0.02	0.01	–
194121	1.98	607	1	5.03	0.022	3.65	0.10	2.75	0.08	0.15	0.01	8.3
194473	1.61	634	1,3	0.884	0.067	16.39	7.92	7.76	1.24	1.22	0.41	8.4
196184	2.65	693	1,3	3.21	0.036	8.71	2.60	2.98	0.33	0.41	0.01	8.3
196290	2.59	701	1,2,3,4	19.2	0.045	13.97	4.66	21.00	2.48	0.42	0.01	8.2
201027	2.87	920	1	1.49	0.023	Inf	7.80	—	—	1.35	0.05	—
202378	2.62	972	1	7.26	0.026	7.86	2.05	1.71	0.17	0.29	0.01	8.4
202484	2.32	1839	1	18.3	0.012	5.79	1.63	1.03	0.13	0.37	0.01	8.4
204595	2.87	3306	1	16.0	0.027	3.48	0.04	7.58	0.08	0.04	0.001	8.0
207524 <sup>g</sup>	1.99	1209	1	0.318	0.020	4.60	1.04	4.21	2.22	0.08	0.04	8.2
207888 <sup>g</sup>	3.33	1270	1	0.215	0.013	2.72	0.42	4.89	0.75	0.06	0.04	8.1
207982	2.00	1226	1	1.58	0.010	3.82	0.29	1.53	0.13	0.16	0.01	8.3
208000	2.58	1229	1,2,3	1.569	0.062	10.14	9.02	2.71	16.54	1.19	0.07	8.5
209962	2.23	1325	1,2,3,4	16.6	0.089	5.69	0.48	2.24	0.07	1.40	0.02	8.5
210730	2.23	1351	1	14.0	0.025	3.00	0.08	4.07	0.11	0.09	0.004	8.2
210885 <sup>g</sup>	3.08	1357	1	5.34	0.031	3.87	0.06	5.71	0.08	0.08	0.003	8.1

<sup>a</sup> MIRI Source ID in the SMILES AGN catalog v0.4.2 published in Lyu et al. (2024);

<sup>b</sup> AGN classification method in Lyu et al. (2024): 1 = from SED fitting; 2 = X-ray luminosity; 3 = ratio of X-ray to radio; 4 = optical spectrum. Readers should check Lyu et al. (2022, 2024) for details.

<sup>c</sup> Including slit loss correction;

<sup>d</sup>  $\lambda\lambda$  4969, 5007

<sup>e</sup>  $\lambda\lambda$  6550, 6585

<sup>f</sup> Estimated from O3N2, errors  $\sim 0.2$  dex

<sup>g</sup> Dwarf galaxy,  $\log(M) < 9.5$ .

high mass cases,  $\log(M) \geq 9.5$ , we assume that any infrared excess powered by young stars will have strong PAH emission features, with relatively little emission at wavelengths short of 6  $\mu\text{m}$ . We do not make that assumption for dwarf galaxies, which are discussed in detail in Section 4. We use the spectroscopy to check the star formation rates to compare with the ones deduced in the overall SED fitting to test the robustness of any conclusions from the SED fitting for the presence of AGNs.

*87191*: This is a dwarf galaxy, with  $\log(M) = 8.7$ . The SFR from the extinction-corrected spectrum significantly exceeds that from the SED fit and also falls far above the main sequence (MS); the extinction correction is evidently too large. The SED-determined value puts it in the main sequence. It is object [A] in Figure 1, which nominally puts it barely into the AGN zone; however, if the line ratios are corrected for the typical conditions in the interstellar medium at  $z = 2.15$  by  $\sim 0.2$  dex (Back-

haus et al. 2024, see also Übler et al. (2023)), it would come down  $\sim 0.2$  dex in  $\log([\text{OIII}]/\text{H}\beta)$  and fall right on the boundary. It has a very strong excess above the photospheric emission, by about a factor of two at 2.4  $\mu\text{m}$  (rest), two orders of magnitude at 4  $\mu\text{m}$  (rest), and leveling out toward longer wavelengths. The SED between 3 and 7  $\mu\text{m}$  is much flatter than that of Haro 11, our metric for hot dust powered by star formation (see Section 4). Its infrared appears to be AGN-dominated.

*113325*: This is another dwarf galaxy, with  $\log(M) = 8.1$ . Both the SED fit and the spectrum indicate it has a very low level of star formation ( $< 4 \text{ M}_{\odot} \text{ yr}^{-1}$ ), within or above the MS. Its excess is both too large and too hot for a star forming galaxy (see Section 4.2.3); Figure 2 shows that its excess is significant at wavelengths short of 2  $\mu\text{m}$  (conveniently marked by the Pa  $\alpha$  line at 1.9  $\mu\text{m}$ ). Its infrared is AGN-dominated.

*194121*: The SFR ( $\sim 14 \text{ M}_{\odot} \text{ yr}^{-1}$ ) puts this galaxy in the MS. The infrared for this galaxy is PAH-

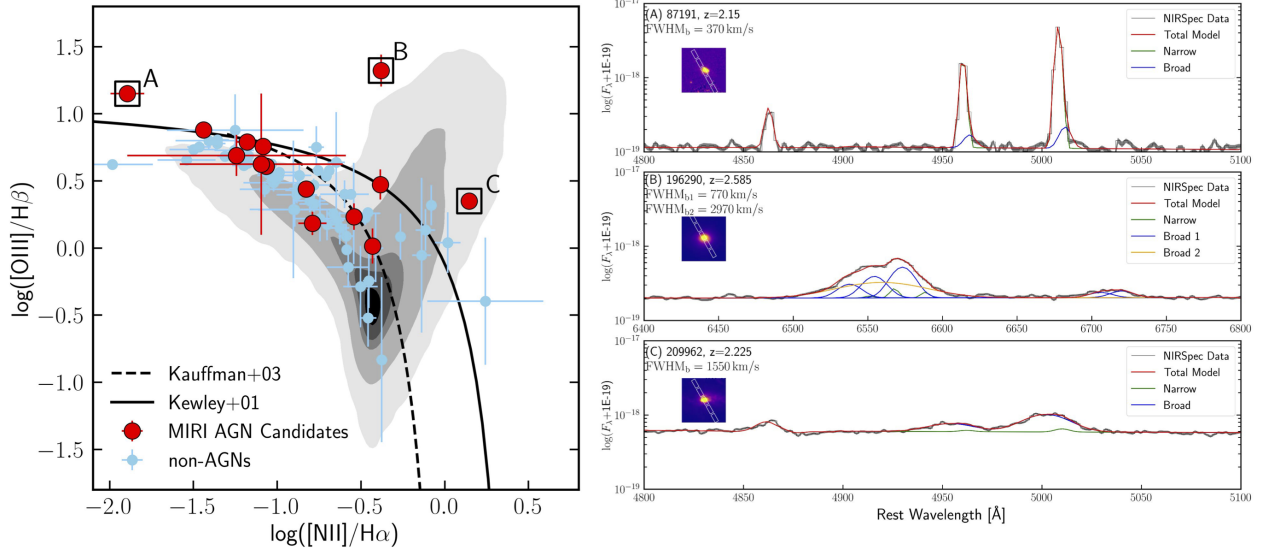


**Figure 1.** Left: Placement of our sample of galaxies on the BPT diagram with lines of demarcation between star forming and active galaxies from Kewley et al. (2001); Kauffmann et al. (2003). The non-AGN spectra are obtained from other galaxies targeted in the SMILES spectroscopy. Right: Spectra of galaxies “A” (87191), “B” (209962), and “C” (196290) marked on the BPT diagram. “A” and “C” have lines broadened by outflows, as shown by the similar widths of the [OIII]  $\lambda$ 4959, 5007 lines to those of the hydrogen lines. “B” appears to be a combination of outflow and broad line AGN.

dominated, although there is a small excess above the purely PAH fit between 4 and 6  $\mu\text{m}$  (rest) that suggests a small contribution from an AGN.

*194473*: This galaxy has a fairly high level of star formation as indicated by both the SED fit and the spectrum ( $\sim 80 M_{\odot} \text{yr}^{-1}$ ), putting it in the MS. It is also relatively bright and massive, with  $\log(M) = 10.7$ . These parameters indicate it should have strong PAH emission, but the data show the PAH contribution to the infrared to be modest, indicating that it is AGN-dominated.

*196184*: This galaxy is at  $z = 2.65$ , but we have a measurement at 25.5  $\mu\text{m}$ . At its mass  $\log(M) = 10.1$ , it should be PAH dominated if it were predominantly star forming and thus have low excess at 5  $\mu\text{m}$  and shorter wavelengths. Although it has a high level of star formation ( $\sim 180 M_{\odot} \text{yr}^{-1}$ ), it has a very substantial excess between 3 and 6  $\mu\text{m}$ , and only a small hint of a PAH feature, requiring the presence of an AGN.

*196290*: The SFR is very high according to both the spectrum and SED fit ( $\sim 100 M_{\odot} \text{yr}^{-1}$ ), and the galaxy is very massive, with  $\log(M) = 11.1$ . Nonetheless its output is overwhelmed by a hot excess from 2 - 6  $\mu\text{m}$  (rest) with only a weak suggestion of PAH features, indicating an obscured AGN. Its spectrum (Figure 1) shows very strong outflows and a possible weak broad line from an AGN. It falls in the AGN region in the BPT diagram, indicating that the AGN is only partially embedded.

*201027*: The  $H\beta$  line is not detected sufficiently well for an extinction correction, but the SED fit indicates

a very high level of star formation ( $\sim 200 M_{\odot} \text{yr}^{-1}$ ). The galaxy is massive, with  $\log(M) = 10.8$  and should be PAH dominated, with little emission from stellar-heated dust short of 5  $\mu\text{m}$ . However, there is a large excess between 3 and 6  $\mu\text{m}$ , indicative of an AGN.

*202378*: The level of star formation is moderately high from the spectrum ( $\sim 35 M_{\odot} \text{yr}^{-1}$ ); we have discounted the extinction-corrected  $H\alpha$ -based SFR because it is implausibly high relative to the MS. We have a 25.5  $\mu\text{m}$  detection, that should pick up PAH emission, but the SED fit (Figure 2) shows a significant hot excess above the expected PAH contribution, indicating an AGN.

*202484*: The extinction-corrected  $H\alpha$  would put this galaxy toward the top of the MS. Both the spectrum and SED fit indicate a moderate level of star formation with no need for an AGN. In Lyu et al. (2024), this source was identified as an obscured AGN assuming a redshift of  $z = 2.32$  from the 3D-HST grism spectrum (grade A). However, our MSA observation yielded a confident spec- $z$  value at  $z = 2.63$ . With the increased redshift, the new SED analysis does not confidently suggest the existence of an AGN. Nevertheless, some excess emission above the galaxy template at  $\lambda$ 4–6  $\mu\text{m}$  can be still seen, indicating the possible existence of a weak AGN.

*204595*: The estimate of the SFR from the SED fit agrees reasonably well with that from the spectrum ( $\sim 100 M_{\odot} \text{yr}^{-1}$ ), putting it near the top of the MS. This galaxy is at a redshift where the PAH bands are shifted out of the MIRI range, but with  $\log(M) = 9.8$  it

**Table 2.** SFR estimates and galaxy masses

ID	z	SFR ( $M_{\odot} \text{ yr}^{-1}$ )	err	SFR ( $M_{\odot} \text{ yr}^{-1}$ )	err	SFR ( $M_{\odot} \text{ yr}^{-1}$ )	log( $M^*$ )
JADES		uncorrected		ext corr		SED fit	$M_{\odot}$
87191	2.15	11.3	0.13	121.4 <sup>a</sup>	28.2	2.5	8.7
113325	2.49	2.75	0.04	3.2	0.8	0.6	8.1
194121	1.98	7.56	0.11	14.4	3.3	2.9	9.9
194473	1.61	0.81	0.13	77	30	79.9	10.7
196184	2.65	9.87	0.17	181 <sup>b</sup>	43	3.0	10.1
196290	2.59	55.7	0.8	3500 <sup>c</sup>	900	339.9	11.1
200525	1.24	2.68	0.04	3.9	0.9	7.3	9.3
201027	2.87	5.56	0.15	—	—	206.8	10.8
202378	2.62	21.65	0.33	303 <sup>d</sup>	72	35.8	9.8
202484	2.63	55.38	1.04	348 <sup>e</sup>	83	5.8	11.1
204595	2.87	59.74	0.65	99	23	40.5	9.8
207524	1.99	0.49	0.03	1.7	0.5	3.0	8.8
207888	3.33	1.15	0.07	1.0 <sup>f</sup>	0.3	2.7	8.6
207982	2.00	2.44	0.06	5.3	1.1	12.0	9.6
208000	2.58	4.54	0.19	123.9	32.5	200.8	10.7
209962	2.23	15.58	0.5	201	48	225.4	10.8
210730	2.23	28.3	0.4	32	7	19.0	9.6
210885	3.08	23.69	0.27	52 <sup>g</sup>	12	1.2	9.4

<sup>a</sup>The H $\alpha$  line uncorrected for extinction puts this galaxy substantially above the main sequence, indicating it is undergoing a starburst. The huge (and highly uncertain) extinction correction is very likely to be overestimated, since it would put the galaxy a factor of  $\sim 100$  above the MS.

<sup>b</sup>The extinction corrected H $\alpha$ -based SFR puts this galaxy modestly above the main sequence, consistent with a starburst.

<sup>c</sup>Both the uncorrected H $\alpha$ -based and the SED-based SFR put this galaxy in the main sequence; the large (and very uncertain) extinction correction to H $\alpha$  would put it an order of magnitude above the MS, which is unlikely.

<sup>d</sup>Both the uncorrected H $\alpha$ -based and the SED-based SFR put this galaxy in the main sequence. The large (and very uncertain) extinction correction to H $\alpha$  would put it an order of magnitude above the MS, which is not likely.

<sup>e</sup>The corrected H $\alpha$  SFR (although highly uncertain) puts this galaxy on the main sequence. The value from SED fitting is well below the MS, which is of course possibly correct also.

<sup>f</sup>The extinction is very small, nominally slightly negative.

<sup>g</sup>The uncorrected H $\alpha$  would put this galaxy in the main sequence and the corrected value would make it a mild starburst.

should be PAH dominated with a resulting weak excess in the 4 - 6  $\mu\text{m}$  range. Nonetheless, There is a strong mid-infrared AGN component.

*207524*: This is a dwarf galaxy with  $\log(M) = 8.81$ . With the update to the redshift and improved photometry (Alberts et al. 2024), what appeared to be a modest mid-infrared excess in Lyu et al. (2024) has disappeared.

*207888*: This is a dwarf galaxy with  $\log(M) = 8.65$ . Its star formation rate is low (**only**  $\sim 1.5 M_{\odot} \text{ yr}^{-1}$ ), from both the spectrum and SED fit, but consistent with the MS. It has a very strong mid-infrared component

starting from 1.5  $\mu\text{m}$  that must be associated with a buried AGN (see Section 4.2.3).

*207982*: The level of star formation is modest ( $\sim 7 M_{\odot} \text{ yr}^{-1}$ ), showing the galaxy lies in the MS. There is a substantial excess in the 5  $\mu\text{m}$  range, confirming that the mid-infrared excess arises from a buried AGN.

*208000*: Both the spectrum and the SED fit indicate ULIRG-level star formation ( $\sim 130 M_{\odot} \text{ yr}^{-1}$ ). The longest wavelength MIRI bands (including 25.5  $\mu\text{m}$ ) are dominated by the PAH emission, but at shorter wave-

lengths the photometry requires an AGN component to boost the output above the pure PAH spectrum.

*209962*: This galaxy has ULIRG-level star formation from both the spectrum and the SED fit ( $\sim 200 M_{\odot} \text{ yr}^{-1}$ ). It also has a lightly obscured AGN whose output is dominant at wavelengths  $> 1.5 \mu\text{m}$ . It has a very high-velocity outflow (Zhu et al. 2025) Figure 1) and the  $H\beta$  detection is weak; these characteristics may hide evidence for a broad line region in our spectrum.

*210730*: Both the spectrum and the SED fit indicate a moderate level of star formation ( $\sim 30 M_{\odot} \text{ yr}^{-1}$ ), which puts it in or near the MS. The longer wavelength MIRI bands are dominated by PAH emission but an additional AGN component is required to fill in at the shorter wavelengths.

*210885*: This is a dwarf galaxy with  $\log(M) = 9.4$ . The spectrum indicates a higher rate of star formation ( $\sim 50 M_{\odot} \text{ yr}^{-1}$ ) than the estimate from SED fitting and the excess attributed to an AGN is seen only at  $\lambda > 3\mu\text{m}$ , where it could be powered by hot stars, so the identification of an AGN is ambiguous.

In summary, we selected a sample with a variety of characteristics to test use of SED fitting to identify obscured AGN in massive galaxies ( $\log(M) > 9.5$ ). The results generally confirm the approach used by Lyu et al. (2024), except where there are errors in redshift. The galaxies ID 87291, 196184, 202484, and 207524 had such errors. For 207524, new modeling at  $z = 1.99$  from our spectrum (instead of a claimed spectroscopic redshift of 1.13) was responsible for the “disappearance” of the obscured AGN compared with Lyu et al. (2024). For 87291, the original modeling was for  $z = 2.48$  from Zeasy (i.e., photometric), but our spectroscopy gave  $z = 2.15$ . Since the correct value is lower, the implications for AGN identification are minor. For 196184 and 202484, the corrected redshifts are increased, 2.08 to 2.65 and 2.32 to 2.63, respectively, but the changes did not undermine the identifications of AGNs. For both of these latter galaxies, the original redshifts were spectroscopic, but our full high signal-to-noise sampling with NIRSPEC leaves no doubt in the new values.

Other than the issues with redshift, the results of this study generally confirm those from SED fitting in Lyu et al. (2024).

#### 4. AGN IN DWARF GALAXIES WITH WARM DUST

We now discuss the selections of AGNs in dwarf galaxies using just SED information, moving beyond the cases with spectra. As shown in Section 3.1, even for massive galaxies, only a small fraction of heavily obscured AGNs can be revealed by optical spectral properties (see also

Lyu et al. 2022). Thus, we need to rely on photometric data to provide a more complete AGN sample for the dwarf galaxy population. The major challenge is that, in contrast to massive galaxies whose star-forming dust emission spectra are well characterized, strong PAH features are no longer universal at the low metallicities of most dwarf galaxies, requiring a re-evaluation of the selection strategy.

Specifically, for low-metallicity systems, dust emission powered purely by hot stars can reach higher temperatures than at solar metallicity (e.g., Draine et al. 2007), because of the hotter stellar UV continua and the different grain properties in low metallicity environment. As a result, low metallicity star-forming galaxies can be confused with AGNs in the near- to mid-IR, as suggested by Hainline et al. (2016); Sturm et al. (2025). However, the number of potentially AGN-impersonating galaxies (hereafter AIGs) in the sample of Hainline et al. (2016) is a very small fraction, as they pointed out. They took their sample from Reines et al. (2013), who found 136 AGN or composite galaxies from a sample of 25974 in the NASA-Sloan Atlas<sup>3</sup>. In their study, Hainline et al. (2016) drew 14013 cases with good WISE detections (median redshift  $z = 0.03$ ), of which 10 fell within the Jarrett et al. (2011) AGN zone in a W2-W3 vs. W1-W2 plot, i.e., only 0.07% of the sample has AGN-like WISE colors. More liberally, if the Stern et al. (2012) line was adopted, 31 sources matched the suggested AGN WISE color, still only 0.2% of the whole population. Other infrared searches for AGN in dwarf galaxies return similarly low identification rates (e.g., Sartori et al. 2015; Mezcuca & Domínguez Sánchez 2024). Such values are probably upper limits, as we will show in Section 4.1 by estimating the fraction of the AIGs that, with more complete spectroscopy, actually *do* have AGNs. We will then discuss galaxy templates that are better suited to fit the low-metallicity galaxy population during AGN identification.

##### 4.1. Spectroscopic evidence for AGNs

In evaluating the overall possibility of mimicking AGNs, it is desirable to assess how likely a dwarf galaxy with warm dust will *not* contain an AGN. To do so, we have focused on the 11 galaxies with AGN-like color and WISE W1  $\gtrsim 14$  in Hainline et al. (2016). The data are less complete and of lower quality for the fainter galaxies, so this selection can give us a small unbiased sample with relatively good measurements. All eleven have reasonably high signal to noise measurements in WISE W3

<sup>3</sup> <https://nsatlas.org/>

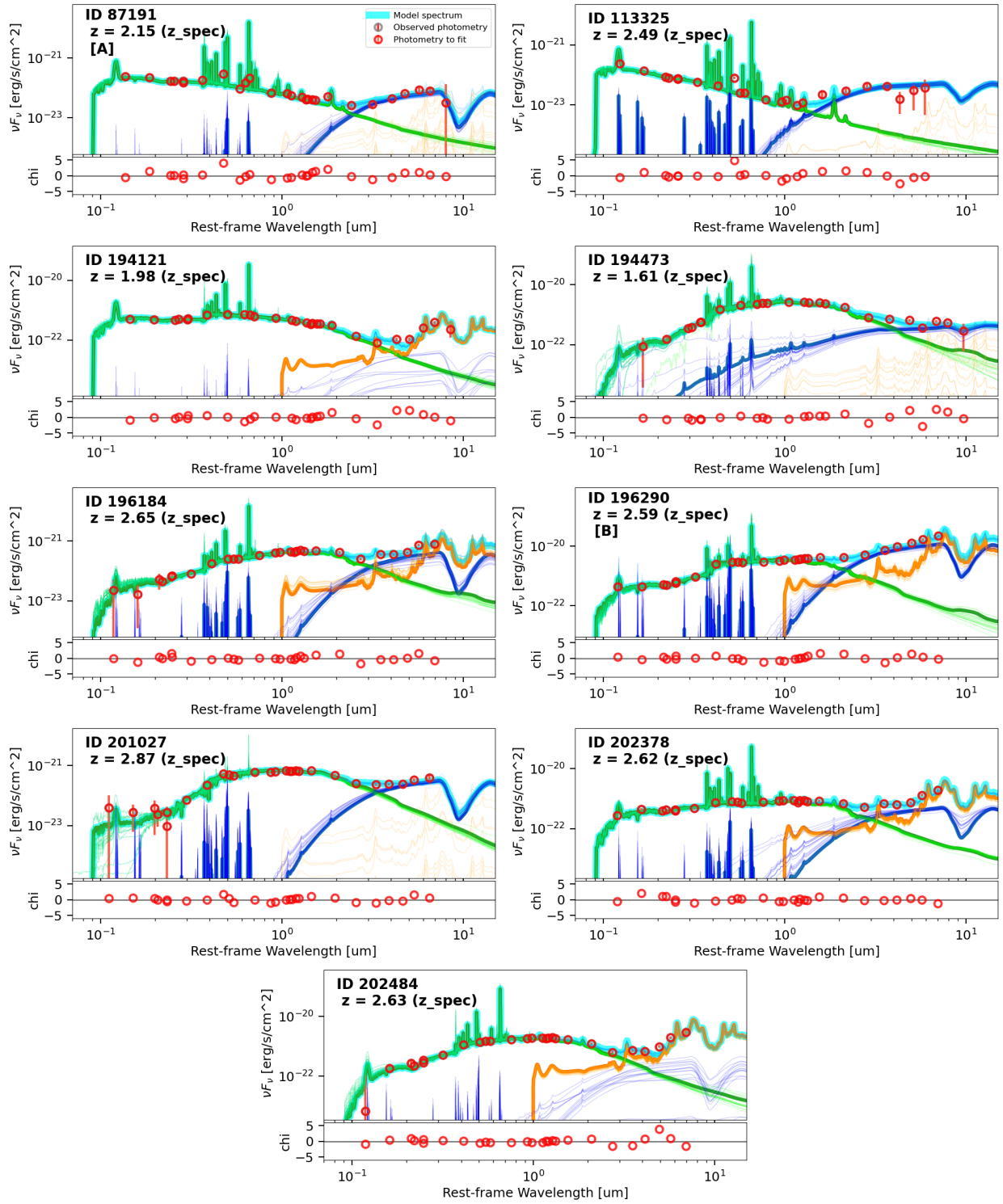


**Figure 2.** Decomposition of photometry into stellar (green lines), AGN (purple lines), and stellar-powered infrared excess (orange lines). We present the galaxy ID and redshift in the top-left corner of each panel. To demonstrate the model degeneracy, we use the light lines to indicate a range of fits that would be acceptable to emphasize that they have little effect on the decision of whether an embedded AGN is present.

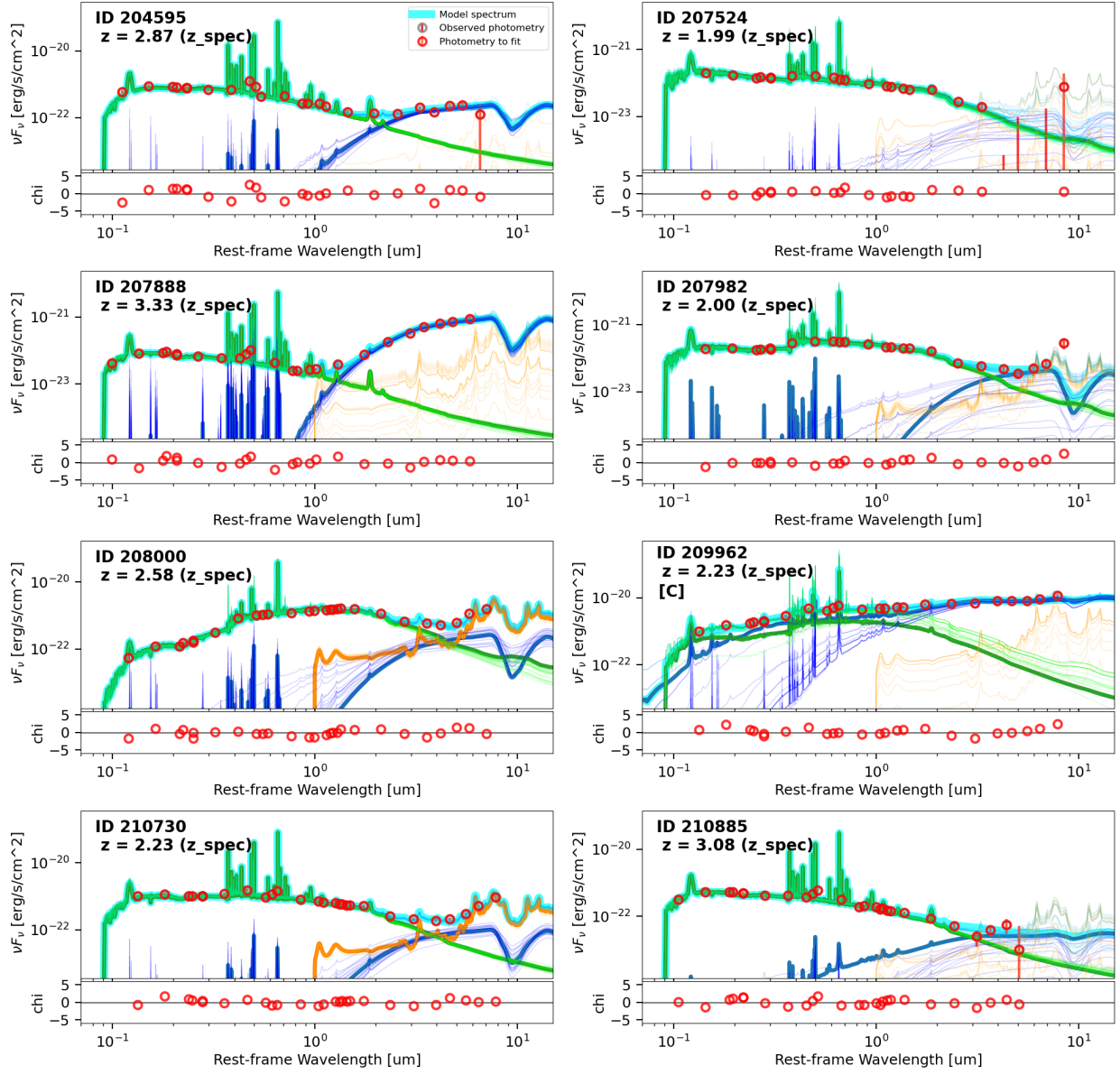


Figure 2. (Continued.)

and W4 and six are detected in the IRAS faint source catalog at  $60 \mu\text{m}$ .

Table 3 shows the result of a literature search for spectroscopic indications of AGN in these 11 galaxies. Of the ten where measurements could be found, six appear to have AGN or are composite. That is, a substantial fraction are not pretending to have AGNs, they actually *have* AGNs. The role of these AGNs in the galaxy infrared emission is not well determined, but they are likely to add flux at the shorter wavelengths and increase the apparent temperature of the “hot” dust. This also suggests that the fraction of false AGN identifications based on mid-IR colors due to very hot dust is likely to be below 0.2%.

#### 4.2. A Broader Perspective

##### 4.2.1. Behavior of dwarf galaxies at high redshift

The sample of Hainline et al. (2016) is all at relatively low redshift, whereas we want to use SED fitting to find AGNs up to the highest redshifts ( $z \leq 3$ ) where extensive photometric MIRI surveys for AGN have been conducted. If the incidence of very high SFR density is much greater at these redshifts, there would be additional false identifications.

Although the star formation rates in massive galaxies decline substantially from cosmic noon to the present, this effect is greatly reduced for dwarfs with a total drop of only  $\times 3$  from  $z \sim 3$  to 0.1 (Förster Schreiber & Wuyts 2020, Figure 4). In addition, the size evolution over this interval is modest (e.g., Mowla et al. 2019; Euclid Collaboration 2025). We therefore expect only a modest increase in the fraction of dwarf galaxies with a very high density of star formation.

##### 4.2.2. Detailed Dwarf Galaxy Properties

Most galaxies studied in Hainline et al. (2016) are faint and relatively little is known about them. To probe the behavior over a sample with better determined properties, we consider the members of the Dwarf Galaxy Survey (DGS) and KINGFISH, which have been studied in detail by Rémy-Ruyer et al. (2013, 2015). So far as is known, none of these galaxies have an AGN of sufficient power to influence its general properties (Rémy-Ruyer et al. 2015).

Rémy-Ruyer et al. (2015) provide aperture-corrected photometry in both the IRAC and WISE bands. Figure 3 shows these galaxies on a WISE color-color plot, similar to that used in Hainline et al. (2016). As they found, few examples appear to be AGN candidates. We have labeled galaxies of interest; they fall into two categories, (1) very low metallicity (I Zw 18, HS0017+1055, and SBS0335-052 with  $12+\log(\text{O}/\text{H})$  of 7.14, 7.63, and

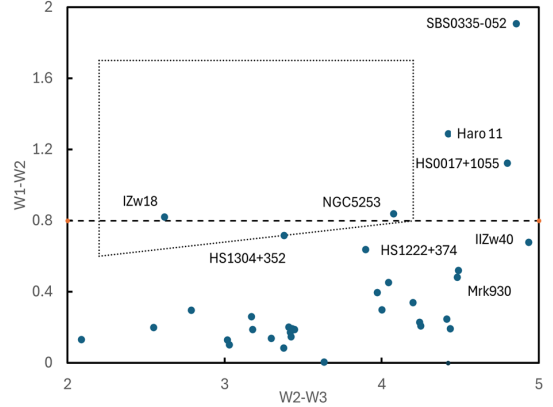


**Figure 3.** WISE color-color plot similar to those used in Hainline et al. (2016) but for the sample of Rémy-Ruyer et al. (2013). The dotted line outlines the AGN zone from Jarrett et al. (2011) and the dashed line is the W1–W2 criterion proposed by Stern et al. (2012)

7.25 respectively (Rémy-Ruyer et al. 2013)) or (2) with very compact nuclear star-forming regions (NGC 5253 (Smith et al. 2020), II Zw 40 (Kepley et al. 2014) and Haro 11 (De Rossi et al. 2018)). However, this diagram provides limited insight for what might be found above  $z = 1$ , since the W3 band shifts to longer observed wavelengths than those of any suitable observations.

Therefore, in Figure 4, we show the IRAC color-color plot proposed by Stern et al. (2005), with the longest band at  $8 \mu\text{m}$ . Donley et al. (2012) demonstrate the validity of this diagram for AGN selections up to  $z \sim 3$ . They also show that the selection region lies along a line, which we show in the figure. This plot adds Tol1214-277, another very low metallicity galaxy with  $12+\log(\text{O}/\text{H}) = 7.52$  (Rémy-Ruyer et al. 2013). Of the seven galaxies in the sample with  $12+\log(\text{O}/\text{H}) \leq 7.63$ , four are within the AGN zone. NGC 930 and II Zw 40 are at the edge of the AGN zone, but they are far from Donley’s optimized zone, so we do not count them as indicated AGNs.

Both color-color plots show that galaxies with very low metallicity, i.e.  $\leq 0.1 Z_{\odot}$ , can have colors, and hence SEDs, that mimic AGNs. They also reinforce the suggestion from Sturm et al. (2025) that very compact nuclear starbursts can have infrared colors similar to those of obscured AGN.

##### 4.2.3. $JHK_S$ colors

We can extend the above investigation to shorter wavelengths using the  $JHK_S$  colors of the galaxies. We have used the photometry in Rémy-Ruyer et al. (2015) to determine standard colors for low metallicity galaxies. We obtain  $J - H = 0.60 \pm 0.03$ ,  $H - K_S = 0.25 \pm 0.03$ , and  $K_S - W1 = 0.34 \pm 0.04$ . We compare these colors with those for the sample with W1-W2 excesses in Hain-

**Table 3.** Indications of AGN in Dwarf Galaxies

SDSS ID	Type	Indicator	Source
J005904.10+010004	SF	BPT, no X-rays	Sturm et al. (2025); Latimer et al. (2021)
J032224.64+401119.8	AGN	BPT, X-rays	Reines et al. (2013); Latimer et al. (2021)
J083538.40-011407.0	AGN <sup>a</sup>	BPT	see note
J090613.75+561015.5	AGN	BPT, brd H $\alpha$ , X-rays	Reines et al. (2013); Kawasaki et al. (2017); Aravindan et al. (2024); Latimer et al. (2021)
J095418.15+471725.1	AGN	BPT, X-rays	Reines et al. (2013); Latimer et al. (2021)
J123948.06-171753.9	29% AGN <sup>b</sup>	BPT	Chen et al. (2022)
J133245.62+263449.3	AGN	BPT, X-rays	Reines et al. (2013); Latimer et al. (2021)
J173501.25+570308.8	composite <sup>c</sup>	brd H $\alpha$	Mezcua & Domínguez Sánchez (2024)
J225515.30+180835.0	–	–	no spectrum available
J231544.60+065439.0	SF	BPT	Wang et al. (2018)
J233244.60-005847.9	SF	BPT	Sturm et al. (2025)

<sup>a</sup>Chen et al. (2022) give a probability of 30% that there is an AGN, but examination of the 6DF spectrum shows that nominally  $\log([\text{OIII}]/\text{H}\beta) \sim 1.6$ , with H $\beta$  weakly if at all detected. This would put the galaxy close to point [B] in Figure 1. The  $3\sigma$  lower limit on  $\log([\text{OIII}]/\text{H}\beta)$  is  $> 1.08$ , while  $\log([\text{NII}]/\text{H}\alpha) \sim -0.2$ , still putting the galaxy into the AGN realm.

<sup>b</sup>Chen et al. (2022) give a probability of 29% that there is an AGN.

<sup>c</sup>Latimer et al. (2021) find the X-ray properties are ambiguous and classify them as “XRB/ULX or AGN,” where XRBs are high-mass X-ray binaries and ULXs are ultraluminous X-ray sources located off the nucleus. For J173501.25+570308.8, Latimer et al. (2021) have no HST image so the X-ray source could be nuclear, which along with its high luminosity (Chen et al. 2022) increases the likelihood that it contains an AGN.

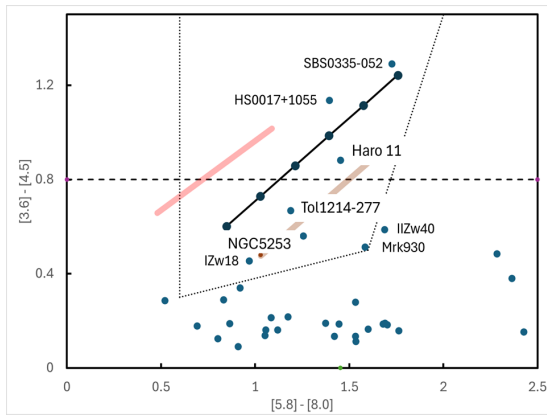


**Figure 4.** IRAC color-color plot for the sample of Rémy-Ruyer et al. (2013). The dotted line outlines the AGN zone from Jarrett et al. (2011) and the dashed line is the W1-W2 criterion proposed by Stern et al. (2012). The dotted line is the refined relation from Donley et al. (2012) and the broad red lines represent the maximum scatter around this relation for 5% errors, which are typical for the measurements plotted.

line et al. (2016). We have used the standard 2MASS point source photometry to focus on the centers of the galaxies. The colors are shown in Figure 5.

Three galaxies stand out in the figure. Number 1 is J123948.06-171753, spectroscopically a star forming galaxy with a modest probability of having an AGN (see Table 3). Despite its relatively red  $J - H$  and  $H - K_S$  colors, its  $K_S - W1$  is 0.45, hardly different from the standard stellar-dominated color. If the red JHK col-

ors were associated with either hot dust or an AGN, we would expect a much redder  $K_S - W1$ . The nature of its behavior is not clear. Galaxies 2 & 3 contain AGNs (Table 3) so their modest red offsets are not necessarily associated with emission by star-heated dust. All the other galaxies are consistent with the standard  $J - H = 0.60$  – and these three cases are also within the errors. This shows that the excess emission identified through the extreme W1-W2 color is gone at  $1.6 \mu\text{m}$ , the effective wavelength of the  $H$  band. That is, the warm dust is not so hot as to emit significantly at this wavelength.

In comparison, for most of the galaxies there *is* excess emission in the  $K_S$  band, showing that the warm dust identified through W1-W2 does have detectable emission at its effective wavelength,  $2.16 \mu\text{m}$ .

#### 4.3. SED of Haro 11 as a template

Previous work has employed the SED of Haro 11 as a template to distinguish embedded AGNs in dwarf galaxies from dust powered by stars (e.g., Lyu et al. 2024). Most of the infrared emission of Haro 11 originates from central knot B, which appears to be a scaled up version of the central clusters in the four AIGs studied by Sturm et al. (2025): diameter  $\sim 140$  pc, young stellar mass  $\sim 3 \times 10^8 M_\odot$  (De Rossi et al. 2018). Its very powerful star formation,  $L \sim 5 \times 10^{10} L_\odot$ , results in an average luminosity density in its interstellar medium  $\gtrsim 10^4 L_\odot \text{pc}^{-3}$ , one of the highest values known among star forming galaxies. Other examples with similarly high lumi-

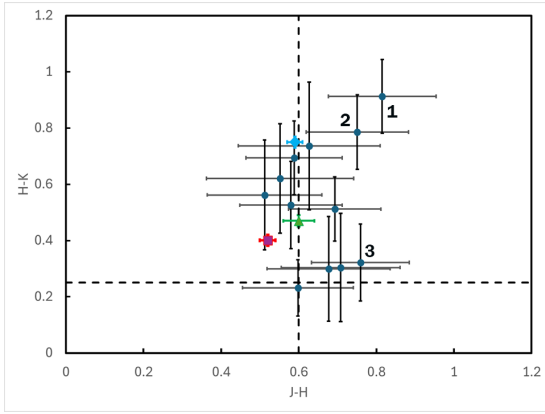


**Figure 5.**  $H-K_S$  vs.  $J-H$  for the subset of AIGs and Haro 11, NGC 5253, and II Zw 40. The standard colors for low metallicity galaxies are shown as dashed lines. An AGN-like excess would lie above the vertical line and to the right of the vertical one. In this case we use the 2MASS point source photometry to focus on the galaxy nuclei and also because it has higher signal to noise than the extended source photometry. The position of Haro 11 is shown as a blue diamond, photometry from [Vader et al. \(1993\)](#); photometry for NGC 5253 is a red square, from the 2MASS extended objects catalog 14'' beam; and II Zw 40 is a green triangle from [Thuan \(1985\)](#). “1” is J123948.06-171753.9, “2” is J032224.64+401119.8 and “3” is J133245.62+263449.3, cases that are discussed in the text.

osity densities have similar infrared SEDs, e.g., NGC 5253, II Zw 40.

All three examples lie near or in the AGN color range in Figure 4, making them representative AIGs. The  $JHK_S$  colors of these three galaxies in Figure 5 show that their dust is sufficiently hot to make  $H-K_S$  slightly red compared with standard colors, particularly true for Haro 11. These results show that Haro 11 is representative of the most extreme star forming dwarf galaxies in terms of its very warm interstellar dust and relatively “hot” SED. Haro 11 is sufficiently luminous that a detailed spectrum is available. This well sampled and high signal-to-noise spectrum is a useful template for this type of behavior. It is very likely that any galaxy with a warmer infrared SED hosts an AGN.

We show the SEDs of 11 potentially AGN-mimicking galaxies in Figures 6 and 7, and compare them with the SED of Haro 11. All the spectra are normalized at WISE W3. The figures make a strong case that the Haro 11 SED is a maximal case for non-AGN galaxies; few if any non-AGN dwarf galaxies are likely to have “hotter” SEDs, i.e., ones with enhanced output in the 3 - 5  $\mu\text{m}$  range. This suggests that the SED of Haro 11 provides a useful *ad hoc* template to use where there is a possibility for stellar-driven warm infrared excesses.

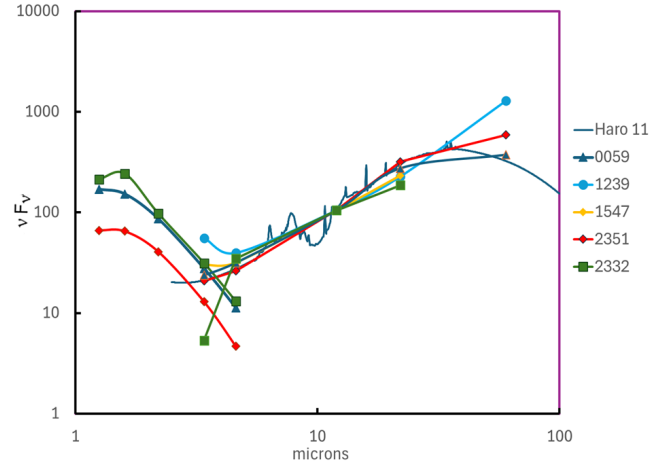


**Figure 6.** Comparison of the SEDs of non-AGN galaxies with that of Haro 11, all normalized at W3. The range from 4 through 12  $\mu\text{m}$  for the dwarf galaxies is matched well by the SED of Haro 11. (We do not show J160135.95+311353.7 because of the lack of  $JHK$  measurements and inconsistencies between the extended and point source photometry.)

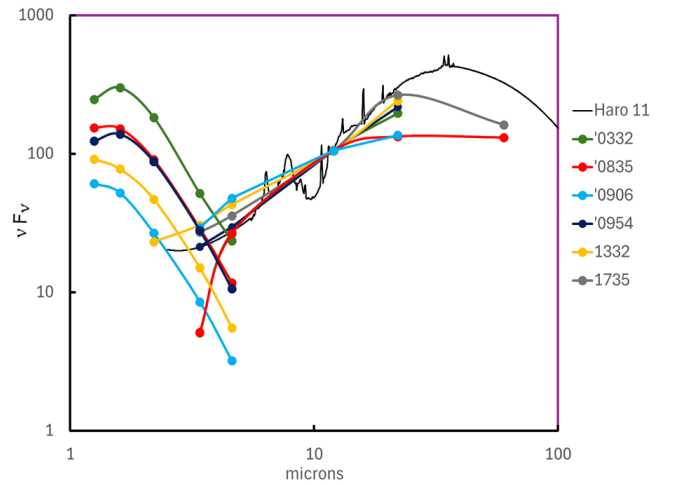


**Figure 7.** Similar to Figure 6 but for the dwarf galaxies with emission line spectra indicating the presence of AGNs. Although the SED of Haro 11 is a good match for some, as anticipated in Section 4.1, three have excesses in the 2 - 5  $\mu\text{m}$  range suggestive of a contribution by their AGNs (J090613.75+561015.5, J133245.62+263449.3, and J173501.25+570308.8)

[De Rossi et al. \(2018, Figure 1\)](#) and [Rémy-Ruyer et al. \(2015\)](#) show how an increasing density of star formation results in more dust heating and a “hotter” infrared SED. They also show that the hot SED of Haro 11 is due to its very dense star formation regions and that this template is a good fit to the galaxies with the highest density of star formation known at  $z > 5$ . It therefore provides a valid limiting hot template for typical galaxies out to  $z = 3$  and beyond.

#### 4.4. Identifying AGNs in more typical dwarf galaxies

So far, we have focused on the dwarf galaxies with the hottest infrared SEDs. These constitute no more than 0.2% of a complete sample of local dwarf galaxies. By adopting the Haro 11 SED as the fiducial template, one may exclude some galaxies containing AGNs to avoid a low level of contamination by non-AGN cases.

It may be possible to improve on this situation by observing the galaxies at wavelengths  $> 12 \mu\text{m}$  (rest). Figure 8 shows how this would work. The SED of a typical AGN flattens past  $10 \mu\text{m}$  and rolls over past about  $25 \mu\text{m}$  (e.g., Lyu & Rieke 2017), while that of star forming galaxies continues to rise to a peak at  $60 - 150 \mu\text{m}$  (e.g., Rémy-Ruyer et al. 2015). In Figure 8, we compare the SEDs of five notorious heavily obscured AGNs with that of Haro 11, and also show the WISE W4 fluxes for eleven dwarfs studied in this paper. All the SEDs are normalized at  $\sim 5 \mu\text{m}$ , i.e., at  $4.6 \mu\text{m}$  for W2 for the WISE photometry and at  $\sim 5.2 \mu\text{m}$  for the obscured AGN spectra. The figure shows a substantially greater relative  $22 \mu\text{m}$  flux (W4) for the star forming galaxies, with a difference already apparent for  $\lambda \geq 12 \mu\text{m}$ . Assuming that an obscured AGN dominates the SED<sup>4</sup>, this difference can be exploited with photometry of relatively narrow bandwidth: WISE W3 is much too broad, but the JWST/MIRI bands are suitable with  $\Delta\lambda/\lambda \sim 0.2$ . The MIRI  $21 \mu\text{m}$  band allows use of this spectral discriminator out to  $z \sim 0.6$ . To exploit this possibility, one also needs photometry to characterize the SED at shorter wavelengths, to detect potentially confusing features such as silicate absorption or PAH emission. The suite of MIRI photometric bands is well suited to doing this. That is, the AGNs in dwarf galaxies can be identified photometrically in a relatively complete fashion using survey data from MIRI providing all the photometric bands, such as the CEERS (Finkelstein et al. 2025) or SMILES (Rieke et al. 2024) surveys. For  $z \gtrsim 0.6$ , we need future IR missions such as PRIMA (Prima Team 2025) to extend the application of such selection techniques to longer wavelengths (Barchiesi 2025).

There are, of course, many other methods to search typical dwarf galaxies for AGN that may escape spectroscopic detection. Messick et al. (2025) have carried out a large-scale search for variability, finding AGN candidates at a 2.4% rate. Birchall et al. (2020) report a similar candidate identification rate from X-ray data. Neither of these approaches will reach any deeply embedded AGN that might be found exclusively in the infrared. However, these studies emphasize the impor-

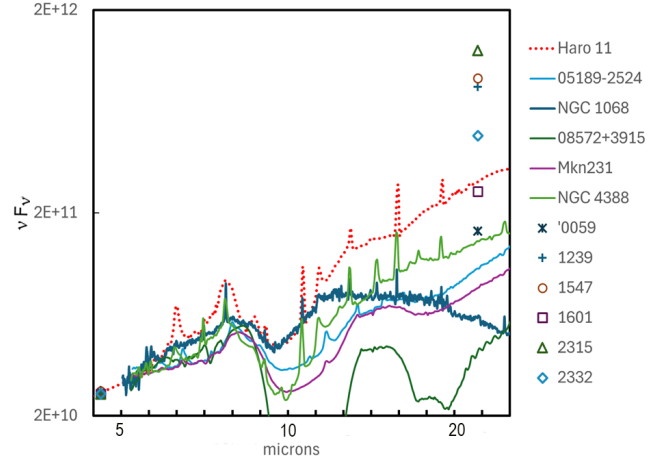


**Figure 8.** Comparison of Haro 11 mid-infrared spectrum with those of heavily obscured AGN examples. The figure also shows the WISE photometry of low metallicity galaxies picked as possible AGN mimics. All the data are normalized at  $\sim 5 \mu\text{m}$ .

tance of multiple approaches to find complete AGN samples, as has been found also for more massive host galaxies.

## 5. DEGENERACIES

There is always a concern with photometric studies such as those discussed here that degeneracies could undermine the conclusions. We discuss this issue from high luminosities to low ones.

Satyapal et al. (2018) discuss whether luminous star forming galaxies could be mistaken for AGN using WISE photometry. They conclude that this is a risk with two-band studies but the problem is largely mitigated if three bands are used. Together NIRCcam and MIRI offer many bands over the WISE spectral range, all of which have been used in Lyu et al. (2024), so we conclude that degeneracy in this range of luminosity is not an issue, so long as a reasonably large suite of the bands offered by JWST is employed.

In the high stellar mass case ( $\log(M_*) \geq 9.5$ ), our distinction between star formation and AGNs depends on two parameters: (1) the presence of PAH emission associated with star formation; and (2) the fitting of the infrared SED with a specific set of semi-empirical models for obscured AGN (Lyu & Rieke 2022). The presence of PAH emission is virtually universal in star forming galaxies above a metallicity threshold that corresponds closely to the mass division between dwarf and massive galaxies (e.g., Marble et al. 2010; Rémy-Ruyer et al. 2015; Shivaie et al. 2024; Whitcomb et al. 2024). In addition, the SED used for an obscured AGN is intrinsically flatter than the typical hot dust emission, so the

<sup>4</sup> All SED-fitting approaches operate under this assumption.

obscured version has a distinct SED shape. In this paper we focused on a small subset of galaxies with extreme luminosity densities, which yields the hottest dust (Rémy-Ruyer et al. 2015). A typical case would have lower temperature dust and a SED falling toward short wavelengths more steeply than the flat part of our assumed AGN SED. Between these two aspects of our modeling, degeneracy for the massive galaxy sample – i.e., mistaking a star forming case for an AGN – should be very low, except at the higher redshifts (e.g.,  $z > 2.5$ ) where our spectral sampling of any infrared excess is limited.

Degeneracy is a risk for dwarf galaxies where PAH emission can no longer be used as the signature of star formation. The conclusion we reach in this paper is that this issue can be avoided if the SED of Haro 11 is used as a limiting template and AGN candidates are only identified on the basis of SEDs with more short wavelength emission than this template.

## 6. CONCLUSION

This paper evaluates a few notable issues that may undermine the identification of AGNs through infrared photometry. For relatively massive host galaxies,  $\log(M) \geq 9.5$ , where the mid-infrared excess powered by star formation should be dominated by PAH features, we find that the major hazard is incorrect redshifts. If the assigned redshift is too low, applying a SED template at that redshift will predict excess emission at relatively short wavelengths. Since the signature of an AGN is excess emission at  $\lambda < 6 \mu\text{m}$ , this can result in false identifications. Otherwise, our high resolution rest-optical spectra behaved as expected, showing star formation for host galaxies with heavily obscured AGN in most cases in rough agreement with the levels assigned through SED fitting of photometry.

We then considered the issue of dwarf galaxies with relatively “hot” infrared excesses, which have been pointed out as mimicking AGNs (Hainline et al. 2016; Sturm et al. 2025). As already pointed out by Hainline et al. (2016), only a very small fraction of dwarf galaxies have such SEDs. We show that the SED of Haro 11 can be used as a limiting template; its SED is as “hot” as the most extreme star forming dwarfs, so any galaxy with a hotter SED is likely to host an AGN (unless it is of extremely low metallicity). However use of this template by itself may exclude some obscured AGNs with Haro 11-like (or cooler) SEDs. This issue can be mitigated by using photometry at  $\sim 13 - 14 \mu\text{m}$  (rest), where true AGN SEDs are turning over while star forming ones are rising toward the far infrared.

## 7. ACKNOWLEDGEMENTS

Work on this paper was supported in part by grant 80NSSC18K0555, from NASA Goddard Space Flight Center to the University of Arizona. This work is based on observations made with the NASA/ESA/CSA James Webb Space Telescope. The data were obtained from the Mikulski Archive for Space Telescopes at the Space Telescope Science Institute, which is operated by the Association of Universities for Research in Astronomy, Inc., under NASA contract NAS 5-03127 for JWST. These observations are associated with program #1207. The specific observations analyzed can be accessed via <https://archive.stsci.edu/hlsp/smiles> and <https://doi.org/10.17909/et3f-zd57>, doi = 10.17909/ET3F-ZD57 <http://archive.stsci.edu/doi/resolve/resolve.html>

*Software:* NumPy (Harris et al. 2020), Astropy (Astropy Collaboration 2013, 2018, 2022), Gelato (Hviding 2022), IDL, Matplotlib (Barrett et al. 2005), TOPCAT (Taylor 2005, 2011).

## REFERENCES

- Alonso-Herrero, A., Poulton, R., Roche, P. F., et al. 2016, MNRAS, 463, 2405. doi:10.1093/mnras/stw2031
- Alberts, S., Lyu, J., Shivaee, I., et al. 2024, ApJ, 976, 2, 224. doi:10.3847/1538-4357/ad7396
- Aravindan, A., Canalizo, G., Secrest, N., et al. 2024, ApJ, 975, 1, 60. doi:10.3847/1538-4357/ad702b
- Astropy Collaboration, Robitaille, Thomas P., Tollerud, Erik J. et al. 2013, *â*, 558, A33, doi = 10.1051/0004-6361/201322068
- Astropy Collaboration, Price-Whelan, A. M., Sipőcz, B. M. et al. 2013, AJ, 156, 123, doi = 10.3847/1538-3881/aabc4f
- Astropy Collaboration, Price-Whelan, A. M., Lim, Pey Lian et al. 2013, ApJ, 939, 167, doi = 10.3847/1538-4357/ac7c74
- Backhaus, B. E., Trump, J. R., Pirzkal, N., et al. 2024, ApJ, 962, 2, 195. doi:10.3847/1538-4357/ad1520
- Barchiesi, L. 2025, Journal of Astronomical Telescopes, Instruments, and Systems, 11, 3, 031609. doi:10.1117/1.JATIS.11.3.031609
- Barrett, P., Hunter, J., Miller, J. T., et al. 2005, Astronomical Data Analysis Software and Systems XIV, 347, 91.
- Birchall, K. L., Watson, M. G., & Aird, J. 2020, MNRAS, 492, 2, 2268. doi:10.1093/mnras/staa040

- Bushouse, H., Eisenhamer, J., Dencheva, N., et al. 2022, Zenodo, 1.8.2. doi:10.5281/zenodo.7325378
- Calzetti, D. 2001, *PASP*, 113, 790, 1449. doi:10.1086/324269
- Chen, Y.-P., Zaw, I., Farrar, G. R., et al. 2022, *ApJS*, 258, 2, 29. doi:10.3847/1538-4365/ac4157
- Chien, T. C.-C., Ling, C.-T., Goto, T., et al. 2024, *MNRAS*, 532, 1, 719. doi:10.1093/mnras/stae1550
- De Rossi, M. E., Rieke, G. H., Shivaee, I., et al. 2018, *ApJ*, 869, 1, 4. doi:10.3847/1538-4357/aaebf8
- Domínguez, A., Siana, B., Henry, A. L., et al. 2013, *ApJ*, 763, 2, 145. doi:10.1088/0004-637X/763/2/145
- Donley, J. L., Koekemoer, A. M., Brusa, M., et al. 2012, *ApJ*, 748, 2, 142. doi:10.1088/0004-637X/748/2/142
- Draine, B. T., Dale, D. A., Bendo, G., et al. 2007, *ApJ*, 663, 2, 866. doi:10.1086/518306
- Euclid Collaboration, Quilley, L., Damjanov, I., et al. 2025, arXiv e-prints, arXiv:2503.15309. doi = 10.48550/arXiv.2503.15309,
- Finkelstein, S. L., Bagley, M. B., Arrabal Haro, P., et al. 2025, *ApJL*, 983, 1, L4. doi:10.3847/2041-8213/adbbd3
- Förster Schreiber, N. M. & Wuyts, S. 2020, *ARA&A*, 58, 661. doi:10.1146/annurev-astro-032620-021910
- Hainline, K. N., Reines, A. E., Greene, J. E., et al. 2016, *ApJ*, 832, 2, 119. doi:10.3847/0004-637X/832/2/119
- Harris, Charles R., Millman, K. Jarrod, van der Walt, Stéfan J., et al. 2020, *Nature*, 585, 357. doi = 10.1038/s41586-020-2649-2,
- Hickox, R. C. & Alexander, D. M. 2018, *ARA&A*, 56, 625. doi:10.1146/annurev-astro-081817-051803
- Hogg, D. W. 1999, , astro-ph/9905116. doi:10.48550/arXiv.astro-ph/9905116
- Hunt, L. K., Thuan, T. X., Izotov, Y. I., et al. 2010, *ApJ*, 712, 1, 164. doi:10.1088/0004-637X/712/1/164
- Hunter, D. A., Elmegreen, B. G., & Madden, S. C. 2024, *ARA&A*, 62, 1, 113. doi:10.1146/annurev-astro-052722-104109
- Hvinding, R. E. 2022, Zenodo, v2.5.2. doi:10.5281/zenodo.7439084
- Jakobsen, P., Ferruit, P., Alves de Oliveira, C., et al. 2022, *A&A*, 661, A80. doi:10.1051/0004-6361/202142663
- Jarrett, T. H., Cohen, M., Masci, F., et al. 2011, *ApJ*, 735, 2, 112. doi:10.1088/0004-637X/735/2/112
- Johnson, B. D., Leja, J., Conroy, C., et al. 2021, *ApJS*, 254, 2, 22. doi:10.3847/1538-4365/abef67
- Kauffmann, G., Heckman, T. M., Tremonti, C., et al. 2003, *MNRAS*, 346, 4, 1055. doi:10.1111/j.1365-2966.2003.07154.x
- Kawasaki, K., Nagao, T., Toba, Y., et al. 2017, *ApJ*, 842, 1, 44. doi:10.3847/1538-4357/aa70e1
- Kennicutt, R. C. & Evans, N. J. 2012, *ARA&A*, 50, 531. doi:10.1146/annurev-astro-081811-125610
- Kepley, A. A., Reines, A. E., Johnson, K. E., et al. 2014, *AJ*, 147, 2, 43. doi:10.1088/0004-6256/147/2/43
- Kewley, L. J., Dopita, M. A., Sutherland, R. S., et al. 2001, *ApJ*, 556, 1, 121. doi:10.1086/321545
- Kirkpatrick, A., Yang, G., Le Bail, A., et al. 2023, *ApJL*, 959, 1, L7. doi:10.3847/2041-8213/ad0b14
- Koyama, Y., Kodama, T., Hayashi, M., et al. 2015, *MNRAS*, 453, 1, 879. doi:10.1093/mnras/stv1599
- Latimer, L. J., Reines, A. E., Hainline, K. N., et al. 2021, *ApJ*, 914, 2, 133. doi:10.3847/1538-4357/abfe0c
- Li, Q., Conselice, C. J., Adams, N., et al. 2024, *MNRAS*, 531, 1, 617. doi:10.1093/mnras/stae964
- Lyu, J., Alberts, S., Rieke, G. H., et al. 2022, *ApJ*, 941, 2, 191. doi:10.3847/1538-4357/ac9e5d
- Lyu, J. & Rieke, G. 2022, *Universe*, 8, 6, 304. doi:10.3390/universe8060304
- Lyu, J. & Rieke, G. H. 2017, *ApJ*, 841, 2, 76. doi:10.3847/1538-4357/aa7051
- Lyu, J., Alberts, S., Rieke, G. H., et al. 2024, *ApJ*, 966, 2, 229. doi:10.3847/1538-4357/ad3643
- Madden, S. C., Cormier, D., & Rémy-Ruyer, A. 2016, *From Interstellar Clouds to Star-Forming Galaxies: Universal Processes?*, 315, 191. doi:10.1017/S1743921316007493
- Marble, A. R., Engelbracht, C. W., van Zee, L., et al. 2010, *ApJ*, 715, 1, 506. doi:10.1088/0004-637X/715/1/506
- Messick, A., Baldassare, V., Jones, D. O., et al. 2025, *ApJ*, 985, 2, 223. doi:10.3847/1538-4357/adcdff
- Mezcua, M. & Domínguez Sánchez, H. 2024, *MNRAS*, 528, 3, 5252. doi:10.1093/mnras/stae292
- Momcheva, I. G., Lee, J. C., Ly, C., et al. 2013, *AJ*, 145, 2, 47. doi:10.1088/0004-6256/145/2/47
- Mowla, L., van der Wel, A., van Dokkum, P., et al. 2019, *ApJL*, 872, 1, L13. doi:10.3847/2041-8213/ab0379
- Prima Team, arXiv, 2025
- Reines, A. E., Greene, J. E., & Geha, M. 2013, *ApJ*, 775, 2, 116. doi:10.1088/0004-637X/775/2/116
- Rémy-Ruyer, A., Madden, S. C., Galliano, F., et al. 2013, *A&A*, 557, A95. doi:10.1051/0004-6361/201321602
- Rémy-Ruyer, A., Madden, S. C., Galliano, F., et al. 2015, *A&A*, 582, A121. doi:10.1051/0004-6361/201526067
- Rieke, G. H., Alberts, S., Shivaee, I., et al. 2024, *ApJ*, 975, 1, 83. doi:10.3847/1538-4357/ad6cd2
- Sartori, L. F., Schawinski, K., Treister, E., et al. 2015, *MNRAS*, 454, 4, 3722. doi:10.1093/mnras/stv2238
- Satyapal, S., Abel, N. P., & Secrest, N. J. 2018, *ApJ*, 858, 1, 38. doi:10.3847/1538-4357/aab7f8
- Shivaee, I., Alberts, S., Florian, M., et al. 2024, *A&A*, 690, A89. doi:10.1051/0004-6361/202449579

- Smith, L. J., Bajaj, V., Ryon, J., et al. 2020, *ApJ*, 896, 1, 84. doi:10.3847/1538-4357/ab8f94
- Stern, D., Eisenhardt, P., Gorjian, V., et al. 2005, *ApJ*, 631, 1, 163. doi:10.1086/432523
- Stern, D., Assef, R. J., Benford, D. J., et al. 2012, *ApJ*, 753, 1, 30. doi:10.1088/0004-637X/753/1/30
- Sturm, M. R., Hayes, B., & Reines, A. E. 2025, *ApJ*, 979, 1, 36. doi:10.3847/1538-4357/ada02f
- Taylor, M. B., "TOPCAT & STIL: Starlink Table/VOTable Processing Software", 2005, *Astronomical Society of the Pacific Conference Series*, 347, 29, editors Shopbell, P. and Britton, M. and Ebert, R., <https://ui.adsabs.harvard.edu/abs/2005ASPC..347...29T>,
- Taylor, Mark, "TOPCAT: Tool for OPERations on Catalogues And Tables", *Astrophysics Source Code Library*, record ascl:1101.010, 2011, <https://ui.adsabs.harvard.edu/abs/2011ascl.soft01010T>
- Thuan, T. X. 1985, *ApJ*, 299, 881. doi:10.1086/163755
- Übler, H., Maiolino, R., Curtis-Lake, E., et al. 2023, *A&A*, 677, A145. doi:10.1051/0004-6361/202346137
- Vader, J. P., Frogel, J. A., Terndrup, D. M., et al. 1993, *AJ*, 106, 1743. doi:10.1086/116762
- Wang, L.-L., Luo, A.-L., Shen, S.-Y., et al. 2018, *MNRAS*, 474, 2, 1873. doi:10.1093/mnras/stx2798
- Whitcomb, C. M., Smith, J.-D. T., Sandstrom, K., et al. 2024, *ApJ*, 974, 1, 20. doi:10.3847/1538-4357/ad66c8
- Wu, Y., Charmandaris, V., Hao, L., et al. 2006, *ApJ*, 639, 1, 157. doi:10.1086/499226
- Yang, G., Caputi, K. I., Papovich, C., et al. 2023, *ApJL*, 950, 1, L5. doi:10.3847/2041-8213/acd639
- Zhu, Y., Alberts, S., Lyu, J., et al. 2025, *ApJ*, 986, 1, 18. doi:10.3847/1538-4357/add263

## APPENDIX

## APPENDIX

## A. ANALYSIS OF SPECTRA

Here we present the expressions used to estimate the quantities and associated uncertainties reported in Tables 1 and 2. For the  $H\alpha$  Luminosity

$$Lum(H\alpha) = H\alpha_{obs} \times 4\pi DL(z)^2 \quad (A1)$$

where  $Lum(H\alpha)$  is the total luminosity emitted by the galaxy,  $H\alpha_{obs}$  is the line flux obtained by fitting the observed spectrum assuming a Gaussian distribution, and the last term is the total area of a sphere centered on the galaxy, whose radius is the luminosity distance  $DL(z)$  in Mpc derived from the observed redshift (Hogg 1999). The associated uncertainty is estimated by assuming a 1% error on the redshift ( $\delta z$ ) and the flux measurement error:

$$\Delta Lum(H\alpha) = \sqrt{\left(\frac{\delta H\alpha}{H\alpha}\right)^2 + \left(\frac{\delta z}{z}\right)^2} \times Lum(H\alpha). \quad (A2)$$

The observed star formation rate follows the definition of Kennicutt & Evans (2012):

$$SFR = Lum(H\alpha)/cx, \quad (A3)$$

where  $cx$  is a constant such that  $\log_{10}(cz) = 41.27$ , **assuming a Kroupa IMF**. The associated uncertainty is calculated as

$$\Delta SFR = \Delta Lum(H\alpha)/cx. \quad (A4)$$

The internal extinction correction ( $A$ ) is derived using the Balmer decrement  $H\alpha/H\beta$ , following Koyama et al. (2015):

$$A(H\alpha) = 6.53 \times \log_{10} \frac{H\alpha}{H\beta} - 2.98. \quad (A5)$$

which has an estimated uncertainty of  $\Delta A \sim 0.24$  magnitudes (Koyama et al. 2015, equation 3). This allows estimating the intrinsic luminosity of the source:

$$L_{intrinsic} = L(H\alpha) * 10^{(0.4*A(H\alpha))}. \quad (A6)$$

The uncertainty is given by

$$\Delta L_{intrinsic} = \sqrt{(\Delta Lum(H\alpha)/Lum(H\alpha))^2 + (0.24/A(H\alpha))^2} \times L_{intrinsic} \quad (A7)$$

To estimate the star formation rate corrected for extinction  $SFR_{corr}$  we use the intrinsic  $H\alpha$  luminosity, e.g., Domínguez et al. (2013):

$$SFR_{corr} = L_{intrinsic}/cx, \quad (A8)$$

The uncertainty of the extinction-corrected star formation rate  $\Delta SFR_{corr}$  is calculated as:

$$\Delta SFR_{corr} = (\Delta Lum(H\alpha) + Lum(H\alpha) \times 0.4 \times \ln(10) \times \Delta H\alpha)/cx. \quad (A9)$$

## B. DISPLAY OF SPECTRA

This appendix displays the NIRSpec MSA spectra used in the first part of the paper.

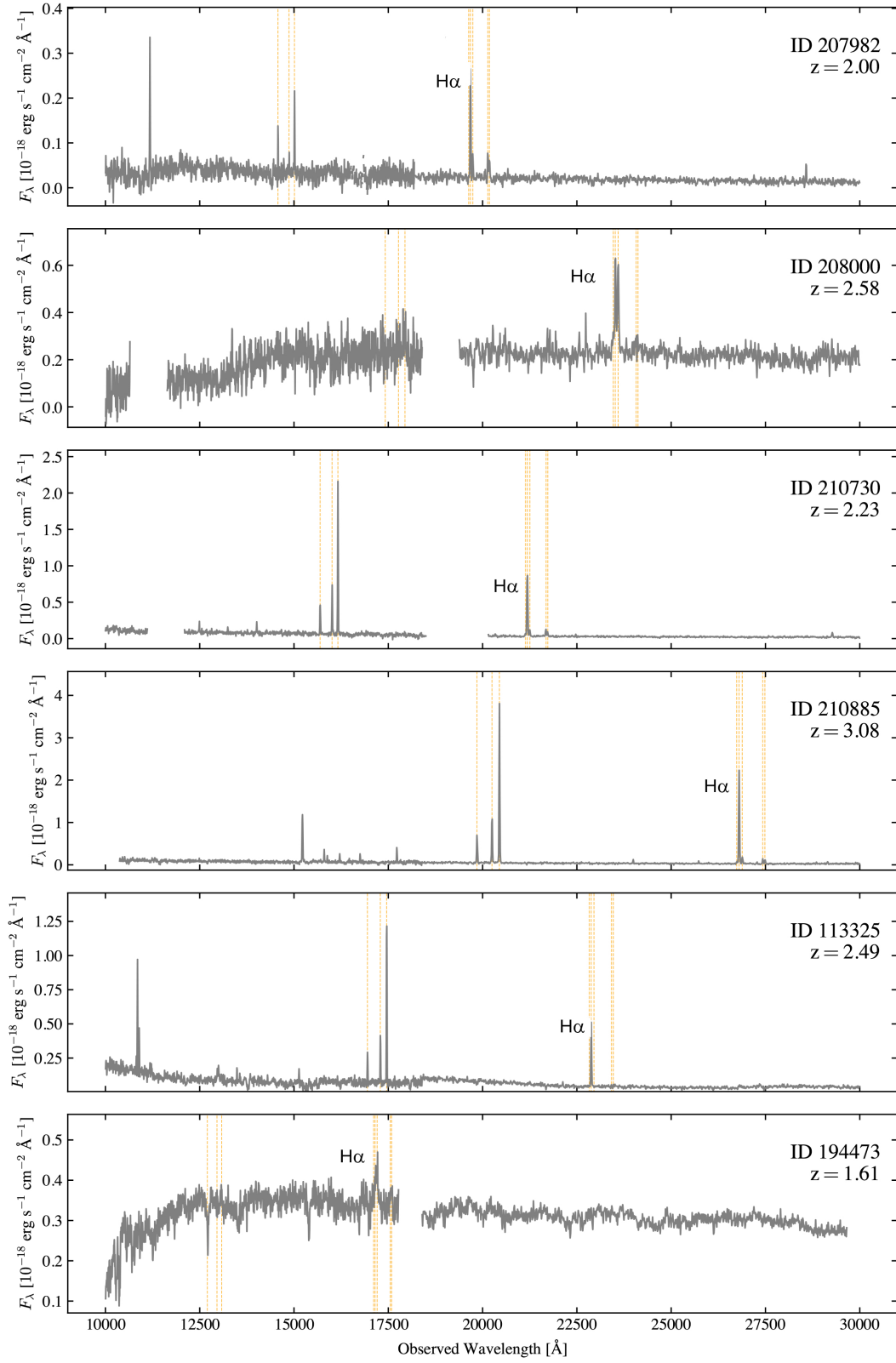


**Figure 9.** Spectra of six of the sources discussed in this paper. The H $\alpha$  lines have been indicated for quick orientation.

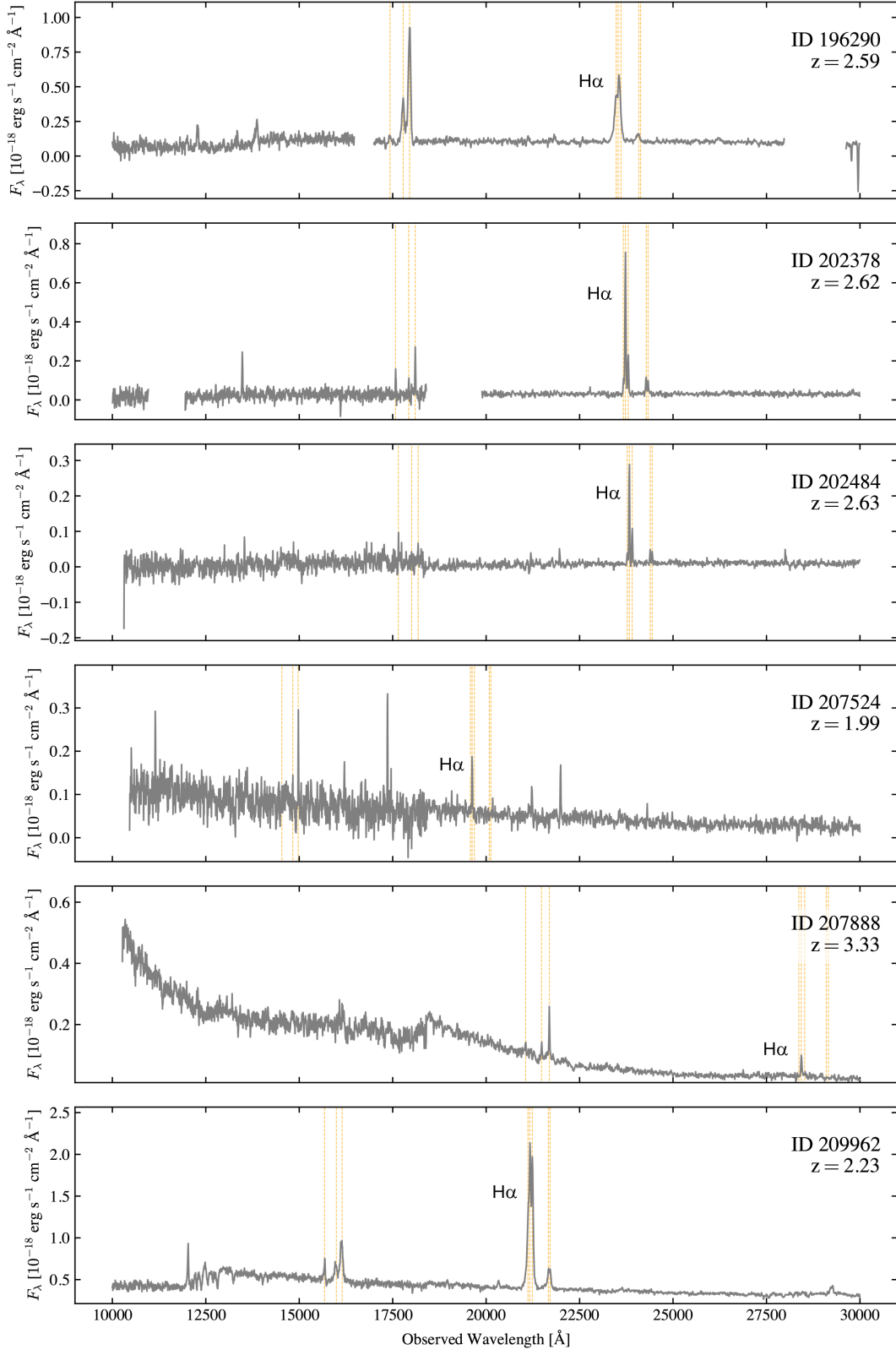


**Figure 9.** continued, spectra of six more of the sources discussed in this paper.

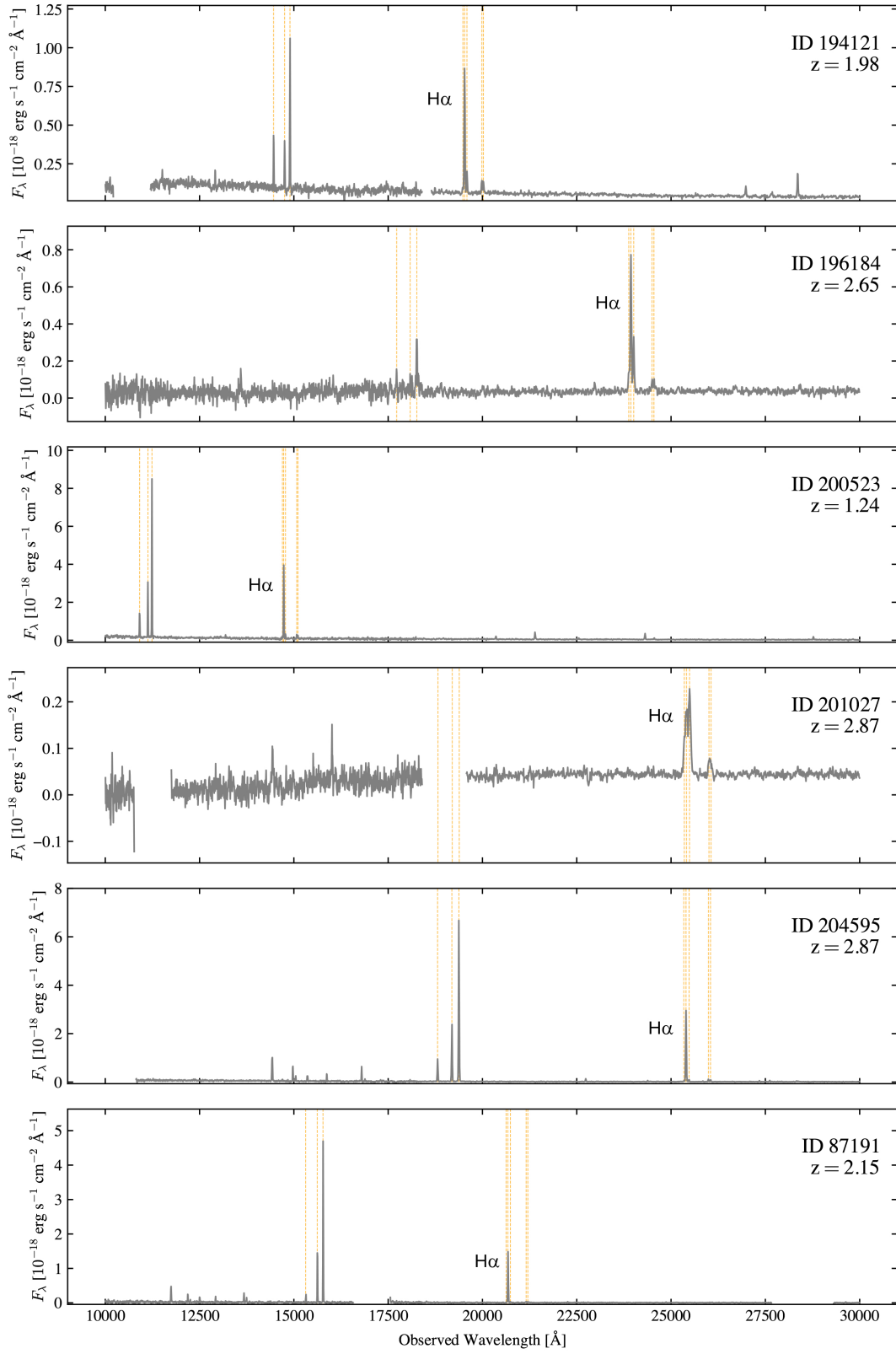


**Figure 9.** continued, spectra of six more of the sources discussed in this paper.